Spat. Inf. Res. (2020) 28(1):113–127
https://doi.org/10.1007/s41324-019-00274-0

Evaluation of topographic correction methods for LULC preparation based on multi-source DEMs and Landsat-8 imagery

Sharad Kumar Gupta[1] · **Dericks P. Shukla**[1]

Received: 9 February 2019 / Revised: 24 May 2019 / Accepted: 28 May 2019 / Published online: 5 June 2019

Abstract Topographic shadows of irregular mountains obstruct the analysis of satellite images in hilly areas. Due to this effect, there is high variability in the reflectance response of similar vegetation types, i.e. sunny areas show more than actual reflectance, whereas shaded areas show less than expected reflectance. In this study, we have evaluated the performance of five topographic correction methods, namely Cosine, C-Huang Wei, semi empirical C, SCS + C and Variable Empirical Coefficient Algorithm (VECA) depending on the solar incidence angle and exitance angle. The two well-known digital elevation models (DEM) i.e. Shuttle Radar Topography Mission (SRTM) and TanDEM-X have been used for the study. The efficiency of the correction methods is assessed on Landsat-8 satellite image using three criteria: visual interpretation, statistical assessment and classification accuracy assessment. As seen from the statistical analysis, VECA and C-correction method provides good correction of topography for both SRTM and TanDEM-X elevation models. We have used support vector machine (SVM) classifier for classification of topographically corrected images. Our results show that VECA and C-correction method increased classification accuracy from 65.60% (for uncorrected image) to 82.40% for SRTM and 64.00% to 80.00% for TanDEM-X respectively. The highest accuracy of classification is obtained using VECA/C method with SRTM DEM. However, the SCS + C-correction method impressively reduced the visual topography effects.

Keywords Topographic correction · Tandem-X DEM · Illumination condition (IL) · Land use land cover (LULC) classification · Support vector machine (SVM)

1 Introduction

The topography of an area plays a significant role in determining the land surface reflectance (which depends on the incident as well as observation angles), which in turn affects the quantitative analysis of multispectral data in the mountainous regions. Terrain orientation varies throughout the topography of an area. It creates variation in the signal received from similar land cover features because of differences in solar irradiance and radiance, according to the angle of incidence, angle of illumination and exitance respectively [1]. Variation in solar illumination angles may cause variations in reflectance of similar ground features, leading to a possible misclassification. In rugged areas variation in reflection geometry and illumination angles are caused by different slope angles and orientations [2]; hence, generating higher radiation in Sun facing slopes and lower in the opposite slopes. In relation to that, mountainous areas having varied topography creates shadows (Fig. 1). In addition, the trees are perpendicular to the geoid and different position of sun illumination causes different shadow effects. As the satellite sensor measures the collective radiance from the features inside their IFOV, the canopy shadowing (and hence the topography) strongly controls the canopy brightness at the pixel scale [3].

Electronic supplementary material The online version of this article (https://doi.org/10.1007/s41324-019-00274-0) contains supplementary material, which is available to authorized users.

✉ Sharad Kumar Gupta
sharadgupta27@gmail.com

Dericks P. Shukla
dericks@iitmandi.ac.in

[1] School of Engineering, Indian Institute of Technology Mandi, Kamand, Himachal Pradesh 175005, India

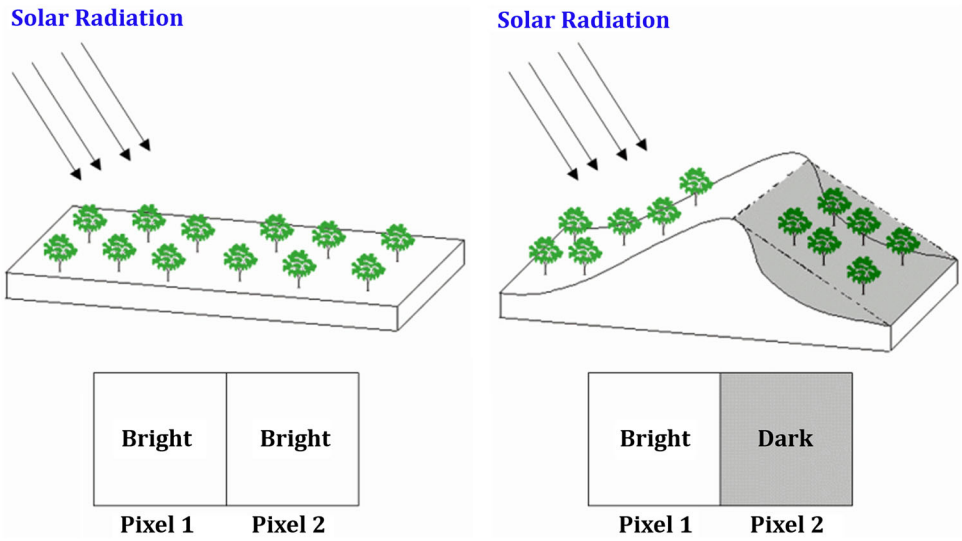

Fig. 1 Effect of Topography on remotely sensed data. In left image, terrain is flat; hence, all the pixels are bright. In right image, terrain is mountainous; hence, shadow effect is present in pixel. (Source: Information extraction using texture analysis, NASA)

This topographic effect can be reduced by various topographic correction methods. These methods can be divided into two type's namely physics based methods and data based empirical methods [4]. The physics based model depend on radiative transfer models and considers the effects of topography as well as atmospheric conditions at the time of acquisition of data [5]. These are very accurate but are highly complicated methods requiring huge amount of observation data. Hence, they are not widely used as getting those parametric data at the time of acquisition is very difficult. So empirical methods are more popular as it uses topographic data such as digital elevation model (DEM) and statistical reflectance information from the satellite images for correction of topographic effects [6, 7]. However, the spatial resolution of DEM plays a critical role in these topographic correction models. It is advised to use a DEM that have similar spatial resolution, as that of the satellite image that needs to be corrected [8–12].

There are various topographic correction models, such as Band ratio and backward radiance correction transformation [2], Minnaert method [2, 13, 14], Cosine correction [7, 11], sun–canopy–sensor (SCS) correction [1, 3, 15], C correction [7, 16]. These have been used widely for correction of topographic effects in Landsat series satellites as well as other satellite images. An empirical method called Variable Empirical Correction Algorithm (VECA) for correction of topographic effects from Landsat 7 ETM + image has also been widely used [17–19].

If the satellite images of mountainous regions are not topographically corrected, and are used for preparation of land-use land-cover classification (LULC), then it will lead to a lot of misclassification. Furthermore, all multi-temporal change detection algorithms depend on comparing an image from different dates assuming that, those images are geometrically corrected & radio-metrically consistent. For radiometric correction of multi-temporal images, topographic correction is especially critical for any study area with rugged terrain, since illumination conditions change along with seasonal sun zenith angle [16]. Hence, before performing any analysis on these satellite images, they must be corrected for topographic effects. Very less work have been carried to study the effect of topographic correction on preparation of LULC in Himalayan areas. In this paper, comparative analysis of five topographic correction methods is carried out and the effect of the best method on LULC is being studied. This will give a suggestion to choose the best topographic correction method for other studies in similar geo-environmental conditions.

2 Data and methodology

2.1 Study area and data resources

Mandi sub-district of Himachal Pradesh, India, is chosen as the study area having the coordinates of 31°41′N Latitude and 76°57′E Longitude. The elevation of the study area varies between 695 m to 2910 m above mean sea level. The slope of study area varies between 0° and 70° with average slope of 21° having standard deviation of 10°. Most of the area present in the south side of the study area has a slope less than 10° whereas the North–North Eastern part has slope ranging between 30 and 45°. Few patches of the study area lie in the 50°–70° slope regimes, which are mostly located on the ridges and peaks. The map of study area is shown in Fig. 2. Mandi is nestled in the Shivalik Range of the Himalayas and has highly rugged topography, which provides an optimal location for topographic correction studies. Landsat 8 satellite image at spatial resolution 30 m was used for carrying out the topographic

correction and Sentinel-2 image at spatial resolution 10 m has been used for validation of classified images after topographic correction. The sun elevation angle is 59.47° whereas the scene acquisition time is approximately 10:53:43 AM for Landsat 8 image. The Landsat-8 image and SRTM DEM was freely downloaded from the United States Geological Survey's EarthExplorer portal (https://earthexplorer.usgs.gov/). TanDEM-X elevation model with spatial resolution 30 m was provided by DLR Germany via TanDEM-X Science Service System (https://tandemx-science.dlr.de). Sentinel-2 image was freely downloaded from European Space Agency's Copernicus open access hub (https://scihub.copernicus.eu/dhus/). The details of the image and DEM used for the region are given in Table 1.

2.2 Image pre-processing

Digital numbers (DN) of satellite images are converted to reflectance values for establishing the relationship between illumination condition value and reflectance of an image for topographic correction analysis. The 12-bit data of Landsat-8 is scaled to 16-bit integers (55,000 grey levels) and is provided in the Level-1 data products. These scaled values are converted to the top of atmosphere (TOA) reflectance using the mathematical formulas (1) and (2) given below [20].

$$\rho_{\lambda'} = M_\rho * Q_{cal} + A_\rho \quad (1)$$

$$\rho_\lambda = \frac{\rho_{\lambda'}}{Sin(\theta)} \quad (2)$$

where $\rho_{\lambda'}$ = TOA Planetary Spectral Reflectance, without correction for solar angle. (Unit less), M_ρ = Reflectance multiplicative scaling factor for the band, A_ρ = Reflectance additive scaling factor for the band, Q_{cal} = Pixel value in DN, ρ_λ = TOA Planetary Reflectance. (Unit less), θ = Solar Elevation Angle (from the metadata).

2.3 Topographic correction

Topographic normalization is performed by modelling illumination condition (IL) with the DEM of same spatial resolution as that of the image to be corrected [21]. The Tan-DEM is used for calculating incident angle (γ_i) which is defined as the angle between the normal to ground and solar beam. IL values varies from -1 to $+1$ [11] where IL < 0 shows shadowed slopes which do not receive irradiance [22]. Angles involved in the calculation of IL are shown in Fig. 3.

The maximum energy incident on a flat surface is obtained when the solar zenith angle is 0° ($\cos\theta_z = 1$; i.e. when the Sun is at nadir). Illumination condition can be calculated using the mathematical Eq. (3) given below.

$$IL = cos\gamma_i = cos\theta_p.cos\theta_z + sin\theta_p.sin\theta_z.\cos(\varphi_a - \varphi_o) \quad (3)$$

where γ_i = local solar incident angle, θ_p = slope angle, θ_z = solar zenith angle, φ_a = solar azimuth angle, φ_o = aspect angle, solar zenith angle $\theta_z = 90$ - Solar elevation.

The following methods as given in Table 2, are then used are used to estimate flat normalized reflectance for each pixel from the computed illumination condition (IL).

Lambertian method assumes that reflectance is independent of observation and incident angle and appears equally bright from all viewing directions [22]. Hence, a Lambertian function corrects only the differences in illumination caused by orientation of the surface. The cosine correction [7] neglects the diffuse irradiance and considers the solar zenith angle and the local solar incident angle for computation of the local illumination. The reflectance of the surface is calculated using the formula given in Table 2. Like Cosine method, C-HuangWei method also follows Lambertian assumption and is wavelength independent. Empirical methods assumes the correlation between radiance recorded in remotely sensed data and illumination condition variable [12]. VECA method was proposed by Gao and Zhang in 2009 [18] and is based on the theoretical and statistical analysis of the reflectance of the image. C-correction method, which was proposed by Teillet et al. 1982 [7], is the modified form of Cosine correction. It uses an empirically defined parameter 'C_k', for the correction of indirect irradiance to the incident solar flux over undulating terrain [18]. In SCS + C correction, the sunlit canopy is projected from the sloped surface to the horizontal in the direction of illumination [1]. In SCS + C and C correction models, we calculate the empirical parameter C_k by exploiting the linear relationship between the illumination condition and the original reflectance. The relation between ρ_T and IL is given in Eq. (4) below.

$$\rho_T = m * IL + b \quad (4)$$

where m and b are slope and intercept of regression line between IL and ρ_T.

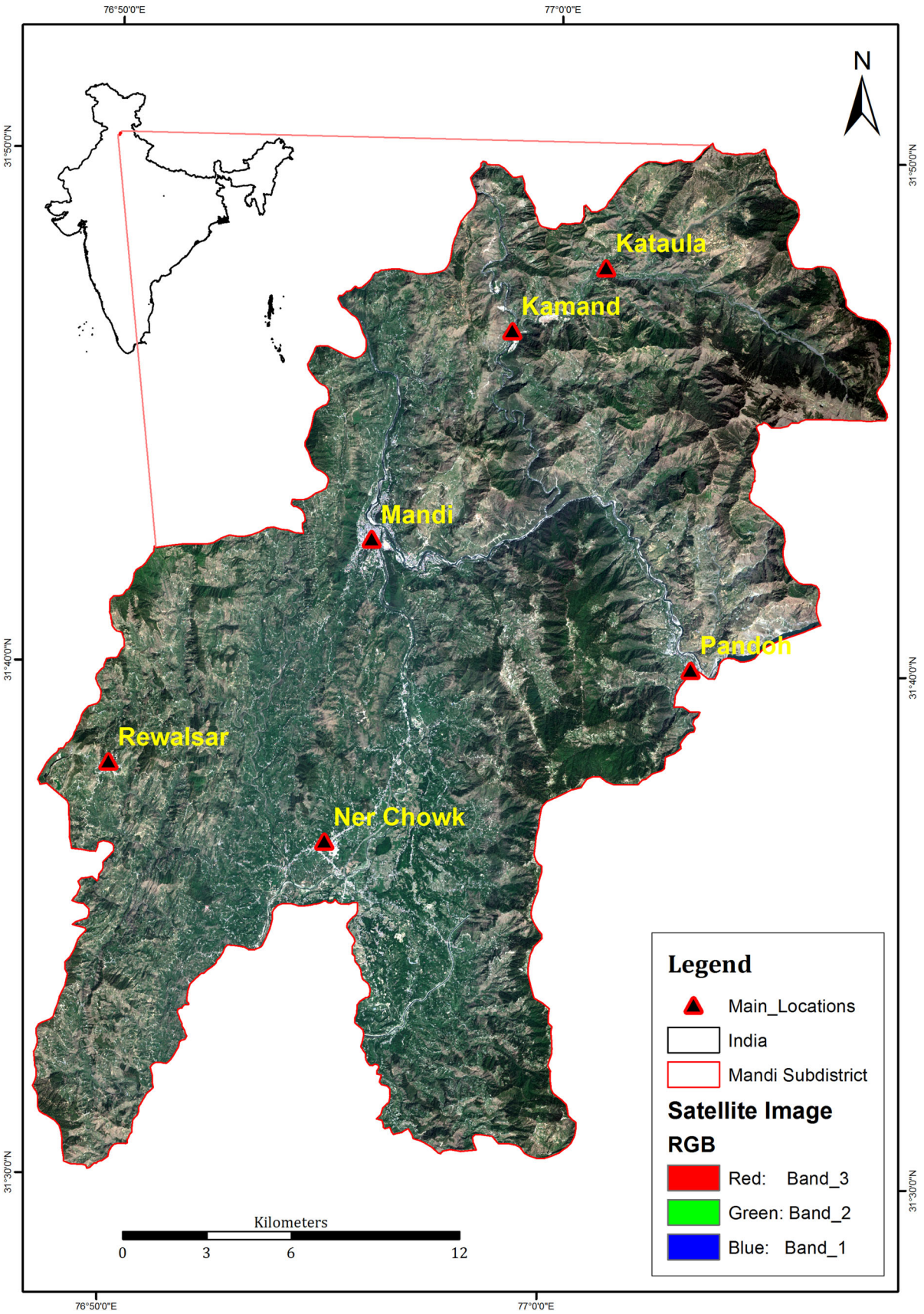
76°50'0"E
77°0'0"E
31°50'0"N
31°40'0"N
31°30'0"N
N
Kataula
Kamand
Mandi
Pandoh
Rewalsar
Ner Chowk
Kilometers
0 3 6 12
Legend
Main_Locations
India
Mandi Subdistrict
Satellite Image
RGB
Red: Band_3
Green: Band_2
Blue: Band_1

◀**Fig. 2** Natural colour composite image of Landsat-8 satellite for the study area of Mandi sub-district, HP, India. [Source: Satellite Image (Earth Explorer, USGS), Boundary of India (Survey of India)]

2.4 Image classification using support vector machine

The images obtained after topographic correction were classified using the training signatures obtained from original satellite image using support vector machine method. The technique consists in finding the optimal separation between the classes in an n-dimensional plane. This method projects linearly non-separable data to a higher dimension using kernel function [23]. The kernel is able to differentiate classes even if the class mean values lies closer to each other. The Fig. 4 shows a simple illustration of the method. The optimal (maximum) margin hyper plane is shown in blue, and the margin between the support vectors is shown by the parallel dotted black lines. The point, which are on the margin, are called support vectors. They are shown as red boxes for class 1, and blue circles for class 2. Let M, $m-dimensional$ training inputs x_i $(i = 1, \ldots, M)$ belong to Class 1 or 2 and the associated labels be $y_i = +1$ for Class 1 and -1 for Class 2. If these data are linearly separable, we can determine the decision function, which is represented by Eq. (5)

$$D(x) = w^T x + b \tag{5}$$

where w and b are weight and bias respectively to map the input into a higher dimensional space. The optimal separating hyperplane (i.e.$D(x) = 0$) is located where the margin between the two classes is maximized, and the misclassification is minimized. The optimal hyperplane satisfies the following constrained minimization as given in Eqs. (6) and (7) below:

$$Min : \frac{1}{2} w^T w \tag{6}$$

$$w^T x_i + b \begin{cases} > 0 & for\, y_i = +1, \\ < 0 & for\, y_i = -1 \end{cases} \tag{7}$$

We can solve the above-constrained optimization problem using the method of Lagrange multipliers and maximizing the Eq. (8) given below:

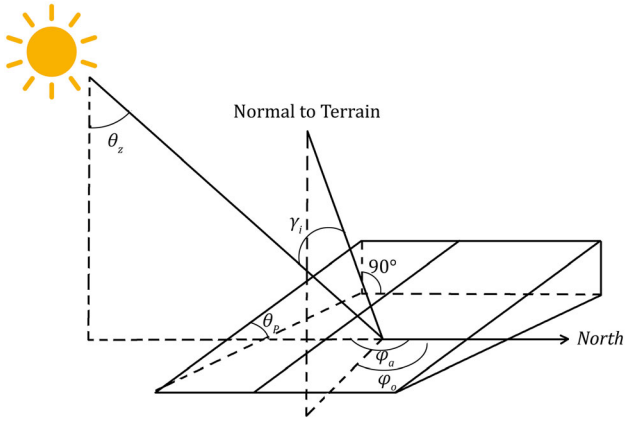

Fig. 3 Angles involved in calculation of illumination condition (IL)

$$L(w, b) = \frac{1}{2}(w.w) - \sum_{i=1}^{m} \alpha_i (y_i (w.x_i + b) - 1) \tag{8}$$

where $\alpha_i = Lagrange`smultiplier$ and $\alpha_i \geq 0$. SVM can perform only binary classification, however classification of data into more than two classes, can be performed using pairwise classification.

2.5 Methodology

Topographic correction requires elevation data for illumination correction over the shadowed regions of the satellite images. DEM should be of similar spatial resolution as that of satellite image. Further, slope angle (in degrees) and aspect angle are calculated from DEM using Horn's method. The parameters required for calculation of illumination condition, such as solar zenith angle, azimuth angle, are taken from metadata provided with the satellite image. Image DN values are converted into top of atmosphere reflectance using the method discussed in *Image Pre-processing step*.

The flat areas do not have any effect of topography hence; they were not included while processing for topographic correction. Flat areas such as reservoirs, lakes, other water-filled areas were demarcated with the help of threshold of normalized difference vegetation index (NDVI) less than zero. While other flat areas such as playgrounds, point-bars, flood plains etc. were identified

Table 1 Data products used in this work

S. no.	Type of data	Resolution (m)	Satellite/mission	Date of acquisition
1.	Satellite image (for processing)	30	Landsat 8	2017-04-13
2.	Digital elevation model	30	TerraSAR TanDEM-X	
3.	Digital elevation model	30	SRTM	
4.	Satellite image (for validation)	10	Sentinel-2	2017-04-10

Table 2 Details of topographical correction methods used in the study

S. no.	Method	Characteristics	Mathematical formula	References
1.	Cosine correction	Wavelength-independent; Lambertian model	$\rho_H = \rho_T\left(\frac{\cos\theta_z}{IL}\right)$	[7]
2.	C-Huang Wei correction	Wavelength-independent; Lambertian model	$\rho_H = \left(\rho_T - \rho_{T_{min}}\right).\left(\frac{\cos\theta_z - IL_{min}}{IL - IL_{min}}\right) + \rho_{T_{min}}$	[27]
3.	VECA correction	Wavelength-dependent; empirical model	$\rho_H = \rho_T\left(\frac{\overline{\rho_T}}{m*IL+b}\right)$	[18]
4.	C-correction	Wavelength-dependent; empirical model	$\rho_H = \rho_T\left(\frac{cos\theta_z + C_k}{IL + C_k}\right)$	[7]
5.	SCS + C correction	Wavelength-dependent; empirical model	$\rho_H = \rho_T\left(\frac{cos\theta_z * \cos\theta_p + C_k}{IL + C_k}\right)$	[1]

where, ρ_H = reflectance of horizontal surface, ρ_T = reflectance of inclined surface, m and b are slope and intercept of regression line between IL and ρ_T and $C_k = {}^{b}/_{m}$

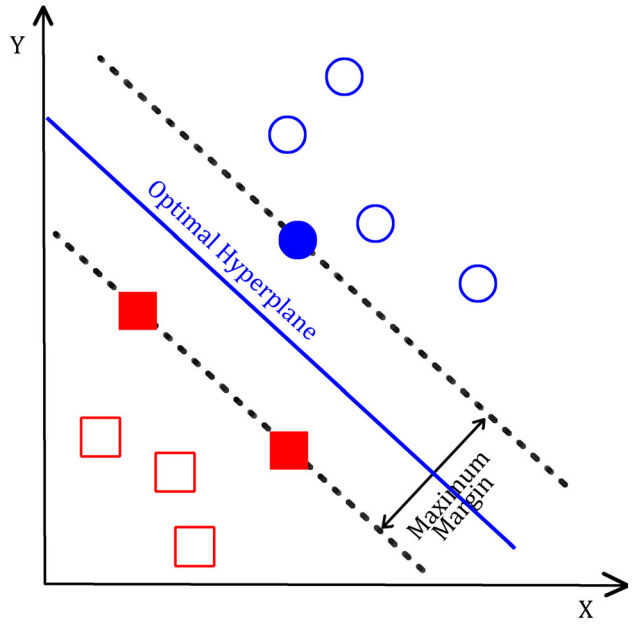

Fig. 4 Illustration of the support vector machine (Taken from OpenCV Tutorial https://docs.opencv.org/2.4/_images/optimal-hyperplane.png)

with slope values less than 1°. In order to create flat area mask, slope was multiplied with NDVI and keeping only positive values. The values below one represent the flat areas whereas the values above one represents non-flat areas.

For finding the band specific correction coefficients for VECA, C and SCS + C methods, linear regression analysis is performed between IL and bands of satellite image (with flat region removed from the image). The slope of regression line shows the effect of topography on the image. After correction of the image, regression analysis is again performed between corrected reflectance value and IL to check the slope of the corrected image. After the topographic correction, the images are classified using support vector machine method. These classified images have been validated using Sentinel-2 image and accuracy assessment is performed. The complete flowchart of the methodology used for topographic correction of Landsat 8 satellite image using SRTM and TanDEM-X digital elevation model is shown in Fig. 5.

2.6 Assessment of topographic correction methods

The performance of the methods was assessed by comparing original Landsat 8 image (Band 2, 3, 4, 5 and 8) and the corrected image using statistical assessment, visual interpretation [13] and using image classification accuracy assessment.

2.6.1 Visual interpretation

Visual interpretation was used for the assessment of the quality of corrected and original image. The visual changes between the corrected image and original image represents the effect of correction. Mostly, we can observe noticeable or small differences in the true colour, false colour composites.

2.6.2 Statistical assessment

The performance of the topographic correction methods is assessed using mean and standard deviation (σ) of individual Landsat-8 bands. A good correction method should decrease the inter-band variability, whereas mean value of each band should be very close to each other [13]. There should be reduction in the relative variability in comparison to the uncorrected image bands. The reduction in topographic shadow effects is shown by change in σ values. Reduction of σ of the reflectance was calculated by the coefficient of variation (CV). CV is the ratio of the σ to the μ, expressed as a percentage as given in Eq. (9) [13].

$$CV(\%) = \frac{\sigma}{\mu} * 100 \tag{9}$$

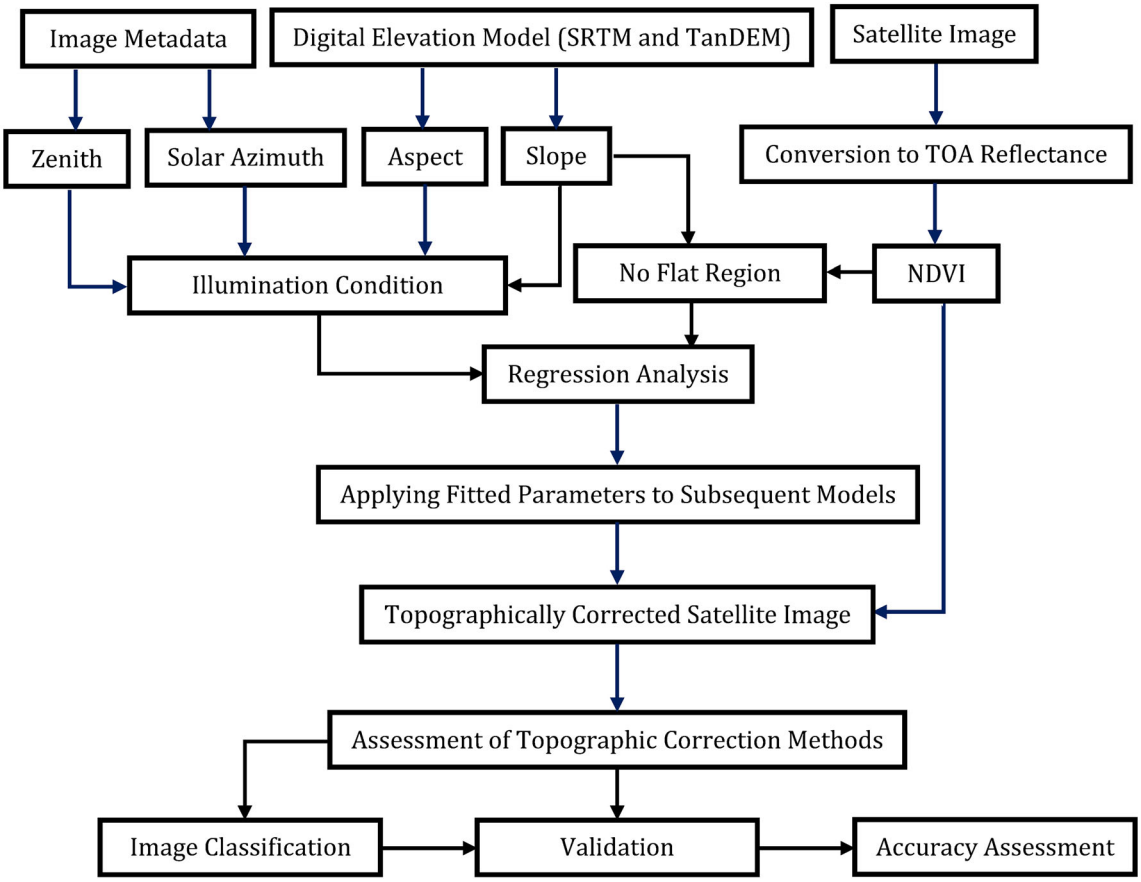

Fig. 5 Flow chart for topographic correction of Landsat 8 satellite images using SRTM and TanDEM digital elevation model

where CV = coefficient of variation, σ = standard deviation of reflectance values, and μ = mean of the reflectance values. After the topographic correction, the CV should decrease.

2.6.3 Image classification accuracy assessment

Accuracy assessment is performed using error matrix, which is computed between ground truth data (reference data) and classified data. An error matrix is a $n*n$ matrix, consisting of values in n rows and n columns. These values expresses the number of testing pixels assigned to a particular category in one thematic classification relative to the number of testing pixels assigned to a particular category in another thematic classification [24]. This matrix represents both the errors of inclusion and error of exclusion present in the classification. Based on the error matrix, we calculate producer's accuracy, user's accuracy and overall accuracy. Once we have error matrix, Kappa analysis can be performed to determine statistically if there is significant difference between two error matrices. The Kappa analysis is a measure of agreement or accuracy, which is based on the difference between the actual agreement in the error matrix (i.e., the agreement between classified data and ground truth data) and the chance agreement, which is indicated by the row and column totals [24, 25].

3 Results and discussions

After the radiometric correction of original Landsat-8 satellite image, we have removed flat areas from the image using SRTM and TanDEM elevation models. The image processed using SRTM elevation model has more area (572.103 sq. km) than the image processed using TanDEM elevation model (561.952 sq. km). The reason for this area difference is because, for both the DEM the generated slope maps are also different and hence the region defined as flat region has different areas. Most of these flat areas are present in the southern portion of the study area as shown in Figs. 6 and 7. In general, these removed flat areas have slope less than 5°. After the removal of flat areas, both the images are processed for topographic correction. The maps produced after application of 5 methods of topographic correction on both SRTM and TanDEM data are

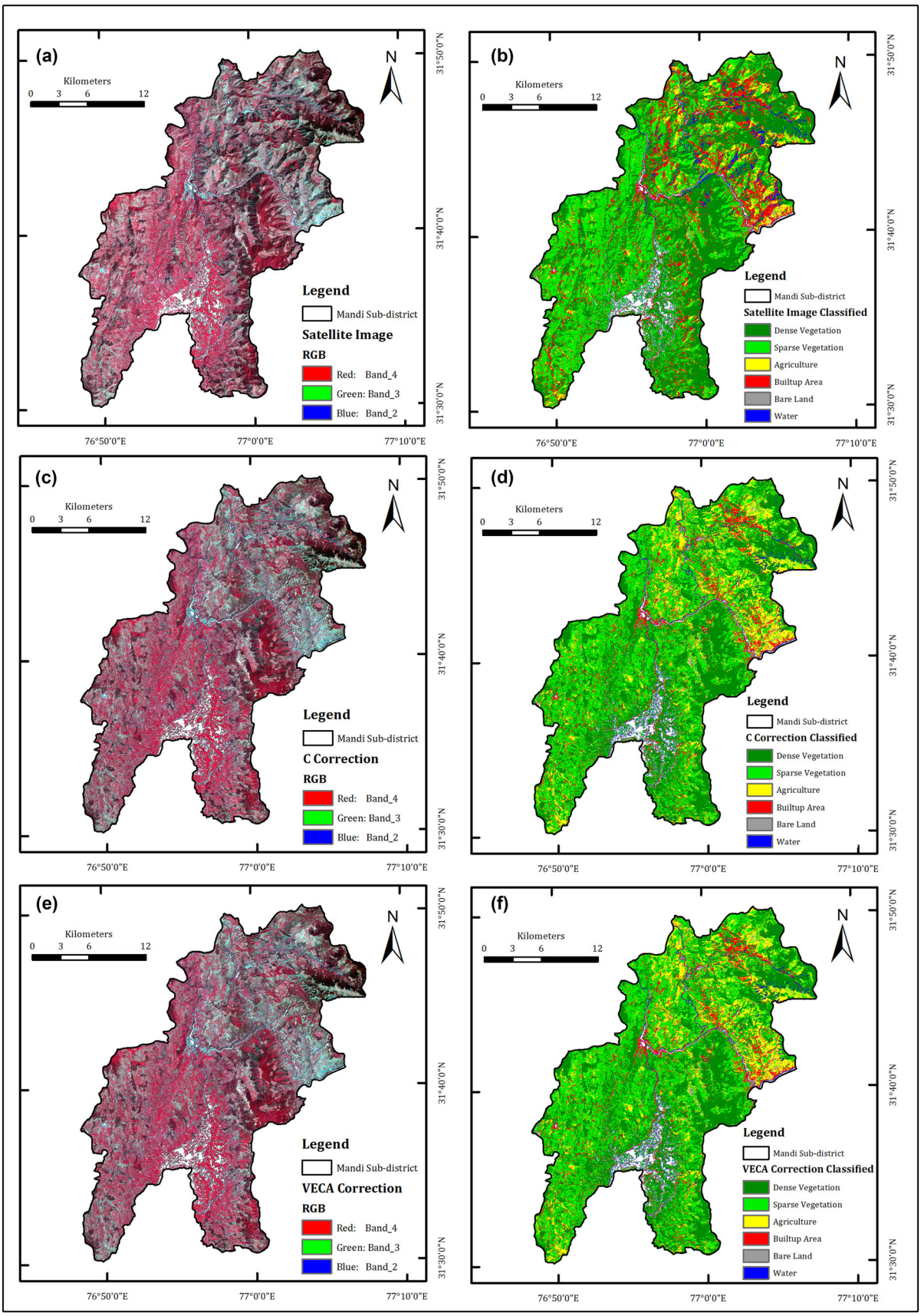
(a)
Kilometers
0 3 6 12
N
Legend
Mandi Sub-district
Satellite Image
RGB
Red: Band_4
Green: Band_3
Blue: Band_2
(b)
Legend
Mandi Sub-district
Satellite Image Classified
Dense Vegetation
Sparse Vegetation
Agriculture
Builtup Area
Bare Land
Water
(c)
Legend
Mandi Sub-district
C Correction
RGB
Red: Band_4
Green: Band_3
Blue: Band_2
(d)
Legend
Mandi Sub-district
C Correction Classified
Dense Vegetation
Sparse Vegetation
Agriculture
Builtup Area
Bare Land
Water
(e)
Legend
Mandi Sub-district
VECA Correction
RGB
Red: Band_4
Green: Band_3
Blue: Band_2
(f)
Legend
Mandi Sub-district
VECA Correction Classified
Dense Vegetation
Sparse Vegetation
Agriculture
Builtup Area
Bare Land
Water
76°50'0"E
77°0'0"E
77°10'0"E
31°50'0"N
31°40'0"N
31°30'0"N

◀**Fig. 6** Maps of the study area using SRTM DEM for correction that show **a** original Image without applying topographic correction; **b** SVM classified map prepared from original image; **c** C-corrected image; **d** SVM classified map prepared from C-corrected image; **e** VECA corrected image and **f** classified map prepared from VECA corrected image

given as supplementary figures (Supplementary Figure 1(a)–6(a) for SRTM and Figure 1(b)–6(b)). The changes can be seen very prominently in various elevated parts of the study area.

A strong correlation exists between the reflectance of pixels in the satellite data and the topographic variable *IL* over rugged terrain. Ideally, for flat terrain the linear regression between image reflectance values and topographic variable $cos\gamma_i$ or *IL* has no slope. If slope exist, it is due to variability of topography. After applying topographic correction methods, spectral differences between original and topographic normalized image should be low, otherwise, it would be a sign of over or under correction. When topographic effects have been corrected, the correlation coefficient of reflectance and *IL* for each band will decrease and similarly, the slope of the fitted line will decrease as shown in Table 3. The scatter plot between reflectance of band 4 and *IL* for original image and all five corrected images using SRTM and TanDEM data is given as supplementary (Supplementary Fig. 7a, b respectively). The equation of regression line and the variation in the slope of the regression line can be seen in this supplementary figure.

It is observed from regression parameters that slope of the regression line between IL & reflectance for VECA method is minimum among all methods. However, there is not much difference in slope obtained from VECA and C methods. The slope obtained after the cosine and C-Huang Wei method is negative whereas positive for remaining other methods. Both of these methods are wavelength independent and does not require any external parameters. They strongly overcorrects the influence of direct irradiance in areas of high incident angles and is therefore problematic for steep and sun-averted slopes, which appear brighter than sun-facing slopes.

The results of the study follow same trend for SRTM and TanDEM data. Small or near zero slope of the regression line indicates better correction. Hence, it can be seen from Table 3 that VECA and C correction has lowest slope i.e. 0.0016 and 0.0017 respectively. This indicates that both these methods perform better and yield nearly similar results. SCS + C also had nearly flat slope indicating good correction. Areas of low illumination are corrected largely. As VECA, C and SCS + C are non-Lambertian methods, which assume that the combination of the angles of incidence and observation can affect reflectance and that surface roughness is an important factor. These methods did not provide any false illumination over any area, which may be also due to the dependency of the methods to the wavelengths.

The mean value of the image should not change much after topographic correction; however, inter-band variability should decrease after correction and hence, coefficient of variation should decrease. Statistics such as mean, standard deviation (SD) and coefficient of variation (CV) are calculated before and after the corrections and they are shown in Table 4. The mean value as well as CV has changed significantly for Cosine method with respect to the original image thus overcorrecting the topographic effects using Cosine method. All the other four methods retained the similar mean value and SD as of original image for all bands. However, out of these five methods, VECA, C and SCS + C has near similar mean and SD with respect to original image and CV has reduced significantly with respect to original image. For C-Huang Wei method, CV has increased thus following the inverse trend. SCS + C method has similar statistics as VECA and C but has higher slope of regression line. Hence, it could be considered as better model then Cosine and C-Huang Wei methods. Finally, it can be ascertained that VECA and C are better performers than other method based on regression parameter as well as statistical indicators. Therefore, from statistical analysis, it can be inferred that VECA and C method are best methods amongst all the discussed methods.

The VECA and C methods obtained from both SRTM and TanDEM data were classified using support vector machine. The images were classified in six land-cover classes' i.e. dense vegetation, sparse vegetation, agriculture, built up, bare land, and water (Figs. 6 and 7). SVM with Radial basis function kernel (Gamma γ = 0.167) has been used for supervised classification of all the images. Total 389 pixels of all the classes were used for training of the model. For accuracy assessment of the classified images, total 250 points were generated and validated using Sentinel-2 image of the study area. These validation points were randomly generated in such a way that those classes such as dense vegetation, sparse vegetation etc. which cover larger areas are not over represented while classes which cover smaller areas such as water, bare land etc. are not under represented. Such type of sampling helps in estimating the overall accuracy and Kappa statistics in more realistic manner. Detailed accuracy assessment is presented in Supplementary Table 1 and Supplementary Table 2. The Table 5 shows classification statistics of all the images. We can see from the Table 5 that water thematic class water occupies 12.308 sq. km (2.151% of study area) and 10.263 sq. km (1.826% of study area) area for SRTM and TanDEM respectively. Although flat areas have been removed from the satellite image, the shadowed areas

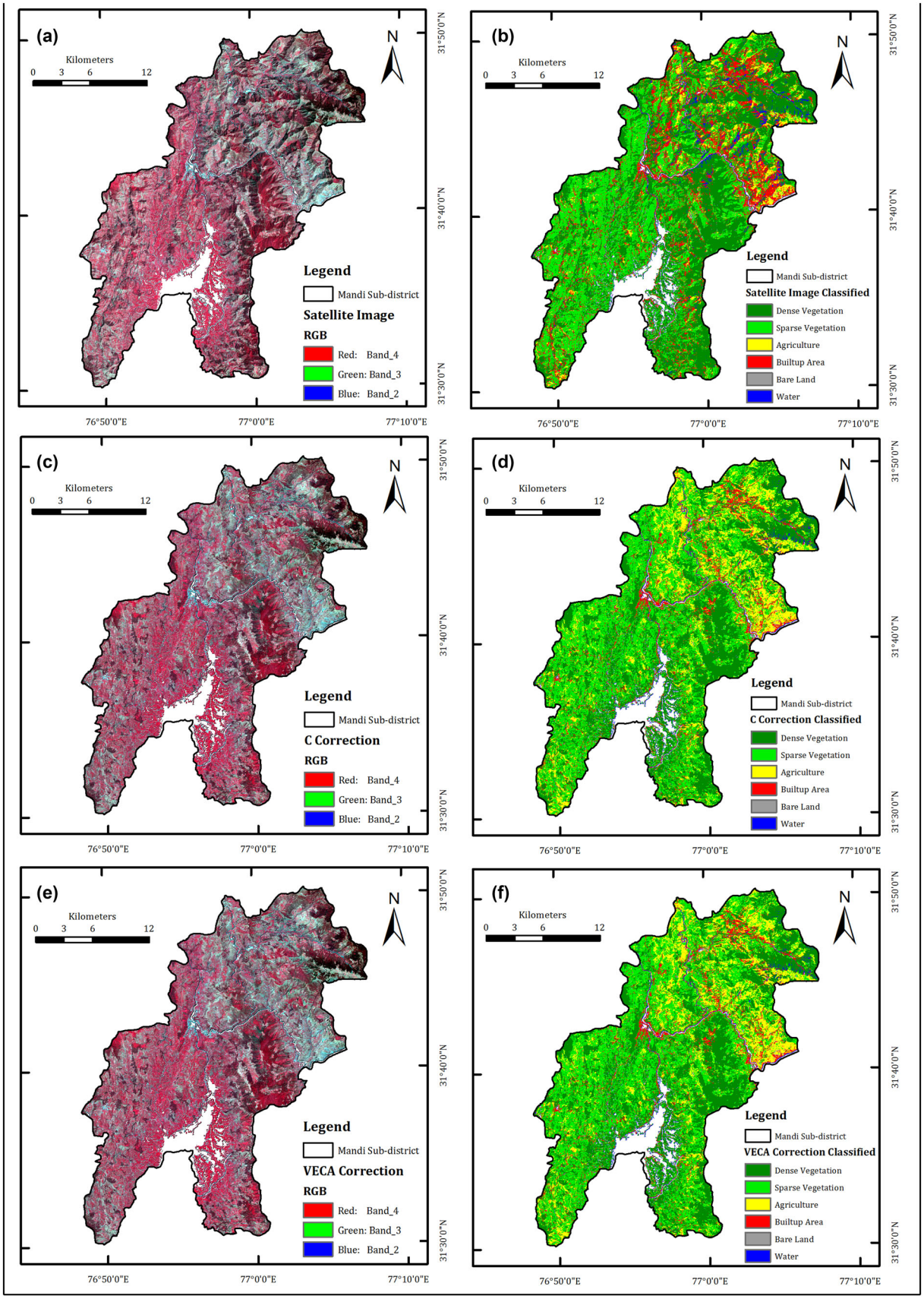
(a)
Kilometers
0 3 6 12
N
Legend
Mandi Sub-district
Satellite Image
RGB
Red: Band_4
Green: Band_3
Blue: Band_2
(b)
Legend
Mandi Sub-district
Satellite Image Classified
Dense Vegetation
Sparse Vegetation
Agriculture
Builtup Area
Bare Land
Water
(c)
Legend
Mandi Sub-district
C Correction
RGB
Red: Band_4
Green: Band_3
Blue: Band_2
(d)
Legend
Mandi Sub-district
C Correction Classified
Dense Vegetation
Sparse Vegetation
Agriculture
Builtup Area
Bare Land
Water
(e)
Legend
Mandi Sub-district
VECA Correction
RGB
Red: Band_4
Green: Band_3
Blue: Band_2
(f)
Legend
Mandi Sub-district
VECA Correction Classified
Dense Vegetation
Sparse Vegetation
Agriculture
Builtup Area
Bare Land
Water
31°50'0"N
31°40'0"N
31°30'0"N
76°50'0"E
77°0'0"E
77°10'0"E

◀**Fig. 7** Maps of the study area using TanDEM for correction that show **a** original Image without applying topographic correction; **b** SVM classified map prepared from original image; **c** C-corrected image; **d** SVM classified map prepared from C-corrected image; **e** VECA corrected image and **f** classified map prepared from VECA corrected image

are classified as water; hence, increasing the area of water thematic class. After topographic correction, the water class occupies only 5.646 sq. km and 5.646 sq. km for VECA and C correction processed using SRTM elevation model, whereas 2.999 sq. km and 2.984 sq. km for VECA

Table 3 Slope and intercept for relation b/w illumination condition and Reflectance (NIR Band) for all correction methods

S. no.	Methods	Parameters (SRTM)		Parameters (TanDEM)	
		Slope (m)	Intercept (b)	Slope (m)	Intercept (b)
1.	Original image	0.2050	0.0679	0.1992	0.0706
2.	Cosine correction	− 0.1383	0.3642	− 0.1542	0.3750
3.	C-Huang Wei correction	− 0.1240	0.3519	− 0.0200	0.2597
4.	VECA correction	**0.0016**	0.2260	**0.0027**	0.2211
5.	C correction	**0.0017**	0.2430	**0.0030**	0.2398
6.	SCS + C correction	0.0354	0.2013	0.0343	0.1992

Bold values emphasize the smallest slope obtained by VECA and C-Correction methods

Table 4 Image statistics showing mean, standard deviation (SD) and coefficient of variation (CV) calculated on all the bands of the original image and after all the corrections used in the study for SRTM data and TanDEM data

Bands/methods	Original image			"Cosine"			"C-Huang Wei"		
	Mean (μ)	SD (σ)	CV	Mean (μ)	SD (σ)	CV	Mean (μ)	SD (σ)	CV
(a) Using SRTM DEM									
Band 1	0.048	0.014	29.543	0.054	0.023	42.221	0.054	0.017	31.629
Band 2	0.063	0.019	30.841	0.070	0.027	37.979	0.070	0.021	30.248
Band 3	0.065	0.026	39.846	0.072	0.032	43.927	0.072	0.027	37.916
Band 4	0.227	0.061	27.030	0.252	0.078	30.890	0.251	0.063	25.070
Band 5	0.179	0.060	33.352	0.198	0.073	36.635	0.198	0.061	30.928
Band 6	0.115	0.047	40.685	0.127	0.054	42.441	0.127	0.048	37.858
(b) Using TanDEM-X									
Band 1	0.047	0.015	32.193	0.054	0.054	99.950	0.051	0.015	30.002
Band 2	0.062	0.021	33.436	0.070	0.056	79.187	0.067	0.020	29.756
Band 3	0.064	0.027	42.040	0.072	0.057	79.053	0.069	0.026	37.871
Band 4	0.223	0.067	29.900	0.252	0.150	59.652	0.242	0.062	25.539
Band 5	0.177	0.063	35.916	0.199	0.131	65.843	0.190	0.059	31.164
Band 6	0.113	0.049	42.911	0.127	0.089	69.857	0.122	0.047	38.259
Bands/methods	"VECA"			"C"			"SCS + C"		
	Mean (μ)	SD (σ)	CV	Mean (μ)	SD (σ)	CV	Mean (μ)	SD (σ)	CV
(a) Using SRTM DEM									
Band 1	0.048	0.013	27.077	0.050	0.014	27.077	0.048	0.013	27.461
Band 2	0.063	0.017	27.441	0.067	0.018	27.441	0.063	0.018	27.819
Band 3	0.065	0.024	36.267	0.070	0.025	36.267	0.065	0.023	36.009
Band 4	0.225	0.052	22.950	0.242	0.056	22.950	0.227	0.055	24.374
Band 5	0.179	0.052	29.202	0.193	0.056	29.202	0.178	0.051	28.781
Band 6	0.115	0.042	36.793	0.125	0.046	36.793	0.115	0.041	36.053
(b) Using TanDEM-X									
Band 1	0.047	0.014	29.564	0.050	0.015	29.564	0.047	0.014	29.926
Band 2	0.062	0.018	29.704	0.066	0.020	29.704	0.062	0.019	30.114
Band 3	0.064	0.024	37.876	0.069	0.026	37.876	0.064	0.024	37.668
Band 4	0.221	0.057	25.565	0.240	0.061	25.565	0.224	0.060	27.039
Band 5	0.176	0.055	31.178	0.192	0.060	31.178	0.176	0.054	30.915
Band 6	0.113	0.043	38.343	0.124	0.048	38.343	0.113	0.043	37.683

Table 5 Class statistics for VECA and C methods with original image, classified for both SRTM and TanDEM data

Classes/methods	Original image (SRTM)		VECA correction (SRTM)		C correction (SRTM)		Original image (TanDEM)		VECA correction (TanDEM)		C correction (TanDEM)	
	Area (sq km)	Percentage	Area (sq km)	Percentage	Area (sq km)	Percentage	Area (sq km)	Percentage	Area (sq km)	Percentage	Area (sq km)	Percentage
Dense vegetation	234.303	40.955	208.247	36.400	208.253	36.401	229.947	40.919	191.720	34.117	191.714	34.116
Sparse vegetation	211.388	36.949	236.669	41.368	236.676	41.369	206.535	36.753	242.051	43.073	242.026	43.069
Agriculture	27.236	4.761	60.309	10.542	60.288	10.538	25.638	4.562	79.467	14.141	79.523	14.151
Built Up	83.939	14.672	53.811	9.406	53.826	9.408	86.936	15.470	44.357	7.893	44.343	7.891
Bare land	2.928	0.512	7.418	1.297	7.414	1.296	2.633	0.469	1.358	0.242	1.361	0.242
Water	12.308	2.151	5.649	0.987	5.646	0.987	10.263	1.826	2.999	0.534	2.984	0.531

and C correction processed using TanDEM elevation model. These results show significant reduction in topographic effects after correction. There is no significant difference in classification results obtained from VECA and C method for SRTM and TanDEM elevation models. This also confirms the results of our statistical analysis of topographic correction methods described above and shown in Table 4.

Error matrix showing producer and user accuracy along with Kappa statistics for Original image, C-corrected image and VECA-corrected image using SRTM and TanDEM are given in Supplementary Tables 1 and 2. The producer's accuracy for sparse vegetation, agriculture and bare land has increased from 0.67, 0.34 and 0.45 for original image to 0.84, 0.90 and 0.73 for VECA and C corrected images using SRTM elevation model, whereas user's accuracy has increased from 0.74, 0.67 and 0.71 to 0.87, 0.68 and 0.73 for the above mentioned classes respectively. While in case of TanDEM corrected images, the producer's accuracy is comparable with that of SRTM corrected image. However, as compared to original image, the TanDEM corrected image has increased producer's accuracy for sparse vegetation, agriculture and built up (from 0.67, 0.31 and 0.60 for original image to 0.86, 0.93 and 0.76 for both VECA and C corrected images). Whereas the user's accuracy has increased from 0.73, 0.56 and 0.32 to 0.81, 0.56 and 0.68 for the above mentioned classes respectively.

From the accuracy assessment results shown in Table 6, we can see that producer's accuracy and user's accuracy for classification results obtained from VECA and C method for SRTM elevation model are same. Similarly, producer's accuracy and user's accuracy are same for classification results obtained from VECA and C method for TanDEM elevation model. Producer and user accuracy for all the classes have improved after topographic correction. After the topographic correction, Kappa coefficient has also increased from 0.54 for original image to 0.76 for VECA and C corrected images for SRTM processing. For TanDEM processing, the Kappa coefficient has increased from 0.52 for original image to 0.73 for VECA and C corrected images. Thus, the correction increases Kappa by 22.35% and 21.14% for SRTM and TanDEM processing respectively. The overall accuracy and Kappa coefficients (unit %) of all classified images are shown in Fig. 8. Considering the overall accuracy of classification, we can observe substantial differences between the original uncorrected data and the terrain-rectified data. As shown in Fig. 8, the overall accuracy of original uncorrected image has increased from 65.60% to 82.40% for corrected imagery using SRTM elevation model, whereas it has increased from 64.00% to 80.00% for TanDEM processing. Thus topographic correction increases overall accuracy by

Table 6 Classification accuracy assessment of VECA and C methods with Original image, classified for both SRTM and TanDEM data

Classes/ methods	Original image (SRTM)			VECA correction (SRTM)			C correction (SRTM)		
	Producer accuracy	User accuracy	Kappa	Producer accuracy	User accuracy	Kappa	Producer accuracy	User accuracy	Kappa
Dense vegetation	0.74	0.81	**0.54**	0.82	0.95	**0.76**	0.82	0.95	**0.76**
Sparse vegetation	0.67	0.74		0.84	0.87		0.84	0.87	
Agriculture	0.34	0.67		0.90	0.68		0.90	0.68	
Built up	0.60	0.32		0.68	0.68		0.68	0.68	
Bare land	0.45	0.71		0.73	0.73		0.73	0.73	
Water	1.00	0.48		1.00	0.65		1.00	0.65	
Classes/ methods	Original image (TanDEM)			VECA correction (TanDEM)			C correction (TanDEM)		
	Producer accuracy	User accuracy	Kappa	Producer accuracy	User accuracy	Kappa	Producer accuracy	User accuracy	Kappa
Dense vegetation	0.73	0.81	**0.52**	0.76	0.97	**0.73**	0.76	0.97	**0.73**
Sparse vegetation	0.67	0.73		0.86	0.81		0.86	0.81	
Agriculture	0.31	0.56		0.93	0.56		0.93	0.56	
Built up	0.60	0.32		0.76	0.68		0.76	0.68	
Bare land	0.27	0.50		0.27	1.00		0.27	1.00	
Water	1.00	0.48		0.91	0.91		0.91	0.91	

Bold indicates the Kappa value of classified images before and after topographic correction. The kappa value increases from 0.54 to 0.76 for SRTM and 0.52 to 0.73 for TanDEM elevation models respectively

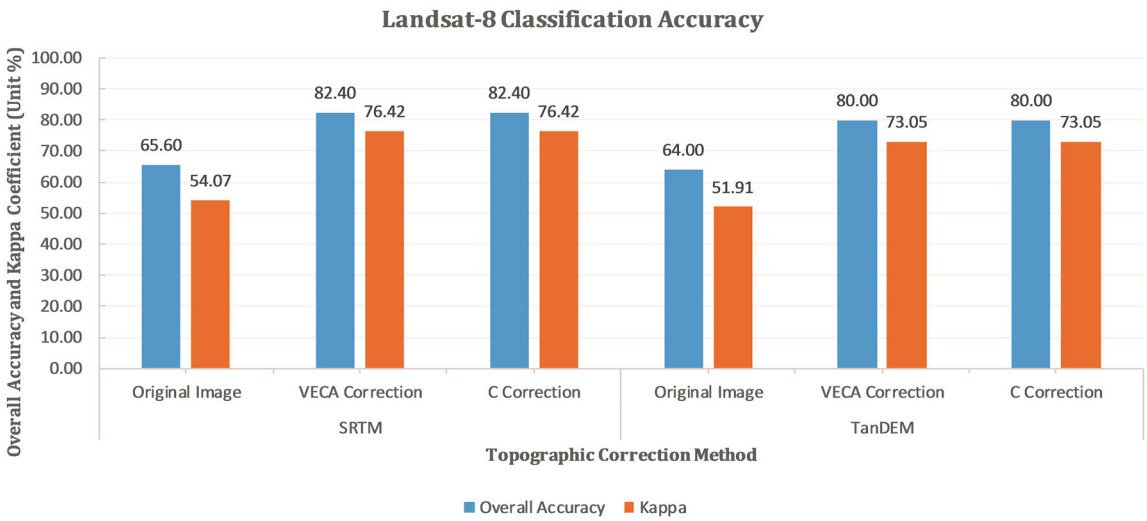

Fig. 8 Overall accuracy and Kappa coefficients of classified results obtained from Landsat-8 images before and after topographic correction using SRTM and TanDEM digital elevation models

16.80% and 16.00% for SRTM and TanDEM processing respectively.

Although the capability of topographic correction methods for elimination of illumination effects in images is debatable [18, 26], the three assessment methods showed that the topographic effects have been removed to different degrees. Topographic correction is largely affected by the availability of a good quality DEM [10, 13]. In this study, the performance of topographic correction varied with respect to the applied correction method and the used

elevation model. The results indicate that VECA correction and C-correction method shows the best performance which is in line with previous studies [8, 13]. Due to the Lambertian reflectance assumptions, the cosine correction method consistently overcorrects the imagery, which is also reported by various other studies [13, 27]. The overall accuracy for classification using the SRTM elevation is higher than the TanDEM elevation model. The SRTM elevation model produced better results compared to the TanDEM for some cover classes such as water and built up. It is evident from our results that classification accuracy increased significantly after topographic correction, which is also reported by various studies [28, 29].

The results show that VECA and C correction methods can be used interchangeably for topographic correction of satellite images of the study area; however, the similar findings cannot be directly applied to other areas. In summary, the accuracy of classification are higher for corrected imagery than that for original uncorrected imagery and the topographic effects can be substantially reduced while increasing the overall accuracy of SVM classification. The results of the study shows the need for topographic correction of satellite images in mountainous areas before preparation of land use land cover maps. This approach can be proven highly suitable for the analysis and detection of long-term change from the Landsat satellites.

4 Conclusions

Based on the comparative analysis, statistical and visual evaluation, we can draw the following conclusions on topographic correction methods performed on the Landsat-8 image for Mandi sub-district region. The Cosine correction have the problem of overcorrection because it does not account for the non-Lambertian nature of the surface to the incident solar illumination and also for the contribution of indirect irradiance, so it is not suitable for correction of topographic effects in highly mountainous terrain as the Himalayas. The remaining methods can be divided into two groups relative to their performance. VECA and C correction performed the best whereas C-Huang Wei and SCS + C correction performed better than the Cosine methods. Both statistically and visually, VECA and C correction have best results in highly rugged terrain. Therefore, it is advised that either of these methods could be applied for topographic corrections of the satellite image of high mountain ranges such as Himalaya. LULC map prepared using VECA ad C correction has highest accuracy (82.40% for SRTM and 80.00% for TanDEM) as compared to non-topographically corrected original image (65.60% for SRTM and 64.00% for TanDEM). A wide variety of methods have been proposed in the literature, however, no methods are universally applicable. In addition, lack of standard and globally accepted models make it difficult to apply topographic corrections. As we see that the topographic effects in satellite images are influenced and determined by many other factors such as adjacent surface, atmospheric condition and land cover, so proper research should be carried out to check applicability of other methods with other images of the similar topography under different illumination conditions (very low sun elevation angle). A good correction method does not change reflectance value significantly but it cannot be applied universally.

Acknowledgements The authors are greatly thankful to German Aerospace Center (DLR) for providing TanDEM-X digital elevation model of the study area through the project (Project No. DEM_-HYDR1925) sanctioned to Dr. Dericks P. Shukla. We would like to thank United States Geological Survey and European Space Agency for providing Landsat-8 and Sentinel-2 images free of cost.

Compliance with ethical standards

Conflict of interest The corresponding author states that there is no conflict of interest.

References

1. Soenen, S. A., Peddle, D. R., & Coburn, C. A. (2005). SCS + C: A modified sun-canopy-sensor topographic correction in forested terrain. *IEEE Transactions on Geoscience and Remote Sensing, 43,* 2148–2159. https://doi.org/10.1109/TGRS.2005.852480.
2. Colby, J. D. (1991). Topographic normalization in rugged terrain. *Photogramm Eng Remote Sensing, 57,* 531–537. https://doi.org/10.1117/12.529775.
3. Gu, D., & Gillespie, A. (1998). Topographic normalization of Landsat TM images of forest based on subpixel Sun-canopy-sensor geometry. *Remote Sensing of Environment, 64,* 166–175. https://doi.org/10.1016/S0034-4257(97)00177-6.
4. Li, H., Xu, L., Shen, H., & Zhang, L. (2016). A general variational framework considering cast shadows for the topographic correction of remote sensing imagery. *ISPRS Journal of Photogrammetry and Remote Sensing, 117,* 161–171. https://doi.org/10.1016/j.isprsjprs.2016.03.021.
5. Balthazar, V., Vanacker, V., & Lambin, E. F. (2012). Evaluation and parameterization of ATCOR3 topographic correction method for forest cover mapping in mountain areas. *International Journal of Applied Earth Observation and Geoinformation, 18,* 436–450. https://doi.org/10.1016/j.jag.2012.03.010.
6. Civco, D. L. (1989). Reduction of the topographic effect in landsat thematic mapper imagery. *Photogrammetric Engineering and Remote Sensing, 55,* 1303–1309.
7. Teillet, P. M., Guindon, B., & Goodenough, D. G. (1982). On the slope-aspect correction of multispectral scanner data. *Canadian Journal of Remote Sensing, 8,* 84–106. https://doi.org/10.1080/07038992.1982.10855028.
8. Gao, Y., & Zhang, W. (2009). LULC classification and topographic correction of landsat-7 ETM + imagery in the Yangjia River watershed: the influence of DEM resolution. *Sensors, 9,* 1980–1995. https://doi.org/10.3390/s90301980.

9. Richter, R., Kellenberger, T., & Kaufmann, H. (2009). Comparison of topographic correction methods. *Remote Sensing, 1,* 184–196. https://doi.org/10.3390/rs1030184.
10. Nichol, J., & Hang, L. K. (2008). The influence of DEM accuracy on topographic correction of Ikonos satellite images. *Photogrammetric Engineering and Remote Sensing, 74,* 47–53. https://doi.org/10.14358/PERS.74.1.47.
11. Riaño, D., Chuvieco, E., Salas, J., & Aguado, I. (2003). Assessment of different topographic corrections in landsat -TM data for mapping vegetation types. *IEEE Transactions on Geoscience and Remote Sensing, 41,* 1056–1061. https://doi.org/10.1109/TGRS.2003.811693.
12. Meyer, P., Itten, K. I., Kellenberger, T., et al. (1993). Radiometric corrections of topographically induced effects on Landsat TM data in an alpine environment. *ISPRS Journal of Photogrammetry and Remote Sensing, 48,* 17–28. https://doi.org/10.1016/0924-2716(93)90028-L.
13. Pimple, U., Sitthi, A., Simonetti, D., et al. (2017). Topographic Correction of landsat TM-5 and landsat OLI-8 imagery to improve the performance of forest classification in the mountainous terrain of northeast Thailand. *Sustainability, 9,* 258. https://doi.org/10.3390/su9020258.
14. Smith, J. A., Lin, T. L., & Ranson, K. J. (1980). The lambertian assumption and landsat data the lambertian assumption I and landsat data. *Photogrammetric Engineering and Remote Sensing, 46,* 1183–1189.
15. Fan, Y., Koukal, T., & Weisberg, P. J. (2014). A sun-crown-sensor model and adapted C-correction logic for topographic correction of high resolution forest imagery. *ISPRS Journal of Photogrammetry and Remote Sensing, 96,* 94–105. https://doi.org/10.1016/j.isprsjprs.2014.07.005.
16. Hantson, S., & Chuvieco, E. (2011). Evaluation of different topographic correction methods for landsat imagery. *International Journal of Applied Earth Observation and Geoinformation, 13,* 691–700. https://doi.org/10.1016/j.jag.2011.05.001.
17. Szantoi, Z., & Simonetti, D. (2013). Fast and robust topographic correction method for medium resolution satellite imagery using a stratified approach. *IEEE Journal of Selected Topics in Applied Earth Observations and Remote Sensing, 6,* 1921–1933.
18. Gao, Y., & Zhang, W. (2009). A simple empirical topographic correction method for ETM + imagery. *International Journal of Remote Sensing, 30,* 2259–2275. https://doi.org/10.1080/01431160802549336.
19. Gao, Y., & Zhang, W. (2007). Variable empirical coefficient algorithm for removal of topographic effects on remotely sensed data from rugged terrain. *International Geoscience and Remote Sensing Symposium, 1,* 4733–4736. https://doi.org/10.1109/IGARSS.2007.4423917.
20. United State Geological Survey (2018) Landsat 8 Data Users Handbook.
21. Jensen, J. R. (2005). *Introductory digital image processing: a remote sensing perspective: Pearson Prentice Hall*. New Jersey: Prentice Hall.
22. Ekstrand, S. (1996). Landsat TM-based forest damage assessment: correction for topographic effects. *Photogrammetric Engineering and Remote Sensing, 62,* 151–161.
23. Shukla, D. P., Gupta, S., Dubey, C. S., & Thakur, M. (2016). Geo-spatial technology for landslide hazard zonation and prediction. In M. Marghany (Ed.), *Environmental applications of remote sensing* (pp. 281–308). Rijeka: InTech.
24. Congalton, R. G., & Green, K. (2008). *Assessing the accuracy of remotely sensed data principles and practices* (2nd ed.). Florida: CRC Press/Taylor & Francis.
25. Congalton, R. G. (1991). A review of assessing the accuracy of classification of remotely sensed data. *Remote Sensing Environment, 4257,* 34–46. https://doi.org/10.1016/0034-4257(91)90048-B.
26. Wu, Q., Jin, Y., & Fan, H. (2016). Evaluating and comparing performances of topographic correction methods based on multi-source DEMs and Landsat-8 OLI data. *International Journal of Remote Sensing, 37,* 4712–4730. https://doi.org/10.1080/01431161.2016.1222101.
27. Gupta SK, Shukla DP (2017) Utilization of Tandem-X Dem for topographic correction of Sentinel-2 Satellite image. In: Pecora 20 -Observing a Changing Earth; Science for Decisions—Monitoring, Assessment, and Projection. Sioux Falls, South Dakota.
28. Vanonckelen, S., Lhermitte, S., & Van, Rompaey A. (2015). The effect of atmospheric and topographic correction on pixel-basedimage composites: Improved forest cover detection in mountainenvironments. *International Journal of Applied Earth Observation and Geoinformation, 35,* 320–328. https://doi.org/10.1016/j.jag.2014.10.006.
29. Tan, B., Masek, J. G., Wolfe, R., et al. (2013). Improved forest change detection with terrain illumination corrected Landsat images. *Remote Sensing Environment, 136,* 469–483. https://doi.org/10.1016/j.rse.2013.05.013.